Impacts of Assimilating High-Resolution Atmospheric Motion Vectors Derived from *Himawari-8* on Tropical Cyclone Forecast in HWRF

MASAHIRO SAWADA

Meteorological Research Institute, Japan Meteorological Agency, Tsukuba, Japan

ZAIZHONG MA

NOAA/National Centers for Environmental Prediction/Environmental Modeling Center/I. M. Systems Group, College Park, Maryland

AVICHAL MEHRA AND VIJAY TALLAPRAGADA

NOAA/National Centers for Environmental Prediction/Environmental Modeling Center, College Park, Maryland

RYO OYAMA

Meteorological Research Institute, Japan Meteorological Agency, Tsukuba, Japan

KAZUKI SHIMOJI

Numerical Prediction Division, Japan Meteorological Agency, Tokyo, Japan

(Manuscript received 3 August 2018, in final form 15 July 2019)

ABSTRACT

The impact of the assimilation of high spatial and temporal resolution atmospheric motion vectors (AMVs) on tropical cyclone (TC) forecasts has been investigated. The high-resolution AMVs are derived from the full disk scan of the new generation geostationary satellite *Himawari-8*. Forecast experiments for three TCs in 2016 in a western North Pacific basin are performed using the National Centers for Environmental Prediction (NCEP) operational Hurricane Weather Research and Forecasting Model (HWRF). Two different ensemble–variational hybrid data assimilation configurations (using background error covariance created by global ensemble forecast and HWRF ensemble forecast), based on the Gridpoint Statistical Interpolation (GSI), are used for the sensitivity experiments. The results show that the inclusion of high-resolution *Himawari-8* AMVs (H8AMV) can benefit the track forecast skill, especially for long-range lead times. The diagnosis of optimal steering flow indicates that the improved track forecast seems to be attributed to the improvement of initial steering flow surrounding the TC. However, the assimilation of H8AMV increases the negative intensity bias and error, especially for short-range forecast lead times. The investigation of the structural change from the assimilation of H8AMV revealed that the following two factors are likely related to this degradation: 1) an increase of inertial stability outside the radius of maximum wind (RMW), which weakens the boundary layer inflow; and 2) a drying around and outside the RMW. Assimilating H8AMV using background error covariance created from HWRF ensemble forecast contributes to a significant reduction in negative intensity bias and error, and there is a significant benefit to TC size forecast.

1. Introduction

Tropical cyclone (TC) forecasts are key in preventing and mitigating their disastrous effects such as torrential rain, violent wind, and storm surge. Although the annual mean TC track forecast error has steadily decreased in the western North Pacific (WPAC) basin since the early 1990s, forecast busts, defined as abnormally large track forecast errors (Yamaguchi et al. 2017), still occur. The TC intensity forecast is also a great challenge since the annual mean intensity errors of the RMSC's official forecast for WPAC has not decreased (e.g., Ito 2016). To improve both the track and the intensity forecast of TCs,

Corresponding author: Masahiro Sawada, msawada@mri-jma.go.jp

DOI: 10.1175/MWR-D-18-0261.1

it is essential to improve the numerical weather prediction (NWP) model for TCs. The Hurricane Weather Research and Forecasting Model (HWRF; e.g., Tallapragada et al. 2014) developed at NOAA/National Weather Service (NWS)/National Centers for Environmental Prediction (NCEP) is one of the state-of-the-art operational TC models. Real-time TC forecasts for the WPAC using the HWRF began in 2012 (e.g., Tallapragada et al. 2015, 2016), and many modifications such as an increase of horizontal resolution (Gopalakrishnan et al. 2012), vortex initialization (Liu et al. 2012), optimization of vertical mixing length (Gopalakrishnan et al. 2013; Zhang et al. 2015), and an ocean coupled system (Kim et al. 2014) have been implemented in the HWRF since then. However, data assimilation, which has been successfully implemented and used in the HWRF for the North Atlantic basin (NATL) and the eastern North Pacific (EPAC) (e.g., Tong et al. 2018), has not been applied in the WPAC yet. The main reason is that observations around the TC are sparser in the WPAC compared to the NATL and EPAC, where aircraft observations such as airborne Doppler radar and dropsondes are available operationally to some degree.

Data assimilation is one of the key components in TC models to allow them to accurately estimate the TC structure and its surrounding environment. While the assimilation of airborne observations have positive impacts on the track (Aberson and Franklin 1999; Aberson et al. 2015; Tong et al. 2018), intensity (Torn 2014; Aberson et al. 2015; Tong et al. 2018), and structure (Pu et al. 2016; Christophersen et al. 2017; Tong et al. 2018) forecasts in regional models, these data are limited in the WPAC. On the other hand, satellite observations or satellite retrieved products such as atmospheric motion vectors (AMVs; Velden et al. 2005), which are derived by tracking clouds or water vapor using consecutive satellite images, are available globally and over the ocean, a generally sparse region for observations. Therefore, AMV data assimilation is very important for the TC forecasts in the research and operational hurricane forecast models.

Previous studies have found that the assimilation of AMVs into the regional models can improve the analyzed TC structures and forecast skill of TC track and intensity. Wu et al. (2014) showed that the initial positions and the timing of the early intensification of Typhoon Sinlaku (2008) were improved in the WRF with an ensemble Kalman filter by adding hourly AMVs into the conventional observations used in the NCEP operational analysis. When the rapid-scan AMVs (RS-AMVs) were added, the ensemble forecasts captured the occurrence of recurvature. A further investigation by Wu et al. (2015) using data-denial experiments indicates the AMVs in the TC's interior and upper layers play an important role in reducing analysis biases and the ensemble spreads of TC position and intensity. Velden et al. (2017) performed a study on the impact of assimilating the high-resolution AMVs on three TCs over the NATL using HWRF. They found that the magnitude of the impact depends on the availability of RS-AMVs and the degree to which unbalanced states are allowed to enter the model analyses through vortex initialization (VI) incorporated in HWRF, though a modest positive impact on track and intensity forecasts can be obtained. Zhang et al. (2018) studied the influence of high-resolution AMVs on the TC forecast with and without VI, and revealed that the assimilation of high-resolution AMVs benefits the track and intensity forecast both with and without the VI. Also, the assimilation of high-resolution AMVs can alleviate the unrealistic vortex modification due to VI, resulting in improved intensity forecasts. Kim et al. (2017) examined the impact of high-resolution AMVs assimilation on TC forecasts using the adjoint-based observation impact method in a framework of observing system experiments. They demonstrated that the forecast error reduction by assimilating the high-resolution AMVs was larger than that by the operational AMVs.

A new generation geostationary meteorological satellite *Himawari-8* became operational at the Japan Meteorological Agency (JMA) in July 2015 (Bessho et al. 2016). The Advanced Himawari Imager on *Himawari-8* has 16 observation bands taken at an interval of 10 min for full disk and an interval of 2.5 min for targeted regions. Yamashita (2016) confirmed that the assimilation of *Himawari-8* AMVs instead of MTSAT2 AMVs has a positive impact on precipitation forecasts by the JMA's operational regional model and on the TC track forecasts by the global model in the framework of OSEs. Kunii et al. (2016) also demonstrated that by taking advantage of the availability of high-frequency observations of targeted regions from *Himawari-8*, the assimilation of RS-AMVs from *Himawari-8* into JMA's operational regional model improved the precipitation forecast. However, the AMVs derived from full disk observations are used in this study as a first step, because the full disk is routinely provided every 10 min without interruption and can be used to monitor more than two TCs at the same time, unlike the targeted region observations. Moreover, the frequency of full disk observations from *Himawari-8* roughly corresponds to that of the rapid scan mode from the previous generation geostationary satellite.

There are several motivations for this study; 1) to extend the previous studies on AMV assimilation over the NATL (Velden et al. 2017; Zhang et al. 2018) to TCs over the WPAC; 2) to evaluate what impacts the high

spatial and temporal resolution (or a large number of) *Himawari-8* AMVs have on the track, intensity, and size of TCs forecasted in HWRF; 3) to explore better ways to make more effective use of the *Himawari-8* AMVs by changing the background covariance used for assimilation.

This paper consists of six sections. Section 2 describes an overview of selected TC cases, the data and methodology used in this study. Section 3 shows statistical verifications of the numerical experiments. We further examine the key processes that are responsible for the different impacts on track and intensity forecasts in section 4. Finally, the summary and discussion of this study are provided in section 5.

2. Data and methodology

a. Himawari-8 *atmospheric motion vector*

The *Himawari-8* AMVs used in this study were derived from three consecutive full disk images taken at 10-min intervals. The motion vectors are retrieved from the tracking of the displacements of clouds in forward and backward. The height of the motion vectors was assigned based on maximum likelihood estimation with observed radiances from *Himawari-8* and the first guess of humidity and temperature profiles from the JMA's global atmospheric model. This algorithm searches for an optimal cloud structure which can explain both the observed radiances and motion vectors by multiple bands. The AMVs were assimilated when the quality indicator (QI; Holmlund 1998) of the AMV data was greater than 0.7. The details of the *Himawari-8* AMVs derivation can be found in the document by Shimoji (2014). The JMA meteorological satellite center (MSC) provides *Himawari-8* AMVs to users hourly.

This study examines the impact of high-resolution AMVs against operational AMVs. The operational *Himawari-8* AMVs (hereafter, OPAMV) are derived at approximately 0.3° by 0.3° if the target box is traceable. The AMV dataset that is used for assimilation by the NCEP operational Global Forecast System (GFS) contains the OPAMV, meaning that it is possible to assimilate *Himawari-8* AMVs into the operational HWRF over the WPAC if the assimilation is turned on. As shown by previous studies (Wu et al. 2014, 2015; Kim et al. 2017; Velden et al. 2017; Zhang et al. 2018), high-resolution AMVs have a positive impact on TC forecasts. Therefore, this study used an experimental dataset of *Himawari-8* AMVs derived for grids with approximately 0.2° by 0.2° resolution at 30 min intervals provided by MSC, which are spatially and temporally higher resolution than was the OPAMV at that time. The high-resolution *Himawari-8* AMVs are called H8AMV hereafter. The same value of observation error is used for OPAMV and H8AMV because the algorithm for AMV derivation and its configuration are the same.

b. HWRF and data assimilation (GSI)

HWRF is an NCEP operational hurricane forecast system and is a triple-nested, atmosphere–ocean coupled system. HWRF version 3.9 used in this study was obtained from the HWRF developers' repository on 1 March 2017. The configuration of HWRF includes the modified NCEP GFS eddy-diffusivity mass-flux (EDMF) as a PBL scheme, a modified Geophysical Fluid Dynamics Laboratory (GFDL) surface layer scheme based on Kwon et al. (2010), the Ferrier–Aligo microphysics parameterization (Ferrier 2005), the scale-aware simplified Arakawa–Schubert scheme (Pan and Wu 1995; Han et al. 2017), and the Rapid Radiative Transfer Model for GCMs (RRTMG) longwave and shortwave radiation scheme (Iacono et al. 2008). The Princeton Ocean Model (POM) that has been adapted to TCs (POM-TC; Yablonsky et al. 2015) was the coupled ocean model employed here, which is different than the Hybrid Coordinate Ocean Model (HYCOM) used for the WPAC in the operational HWRF. The HWRF model consisted of three nested domains with horizontal resolutions of 18, 6, and 2 km. The outermost domain is fixed in time and the two inner nested domains (d02 and d03) follow the predicted storm center. The domain size is 24° × 24° for d02 and is 7° × 7° for d03. There were 61 hybrid vertical levels from the surface to 10 hPa. The details can be found in the HWRF scientific documentation (Biswas et al. 2018).

The atmospheric fields of the outermost model domain were initialized from the GFS analysis. For the nested domains, the fields are derived from 6-h forecasts from the global data assimilation system (GDAS) with VI. The vortex-scale fields originated from the previous 6-h forecast of HWRF when available. In the vortex initialization, vortex intensity and structure are adjusted based on the observed TC parameters provided by the NCEP TC-Vitals (Liu et al. 2012). After the VI, data assimilation using the Gridpoint Statistical Interpolation (GSI) is conducted for the ghost outer and inner nested domains with 6-h cycle to generate a vortex structure in the same way as EPAC and NATL. The data assimilation domains are referred to as "ghost" domains.[1] For the GSI-based ensemble–variational hybrid assimilation, the background error covariance of the hybrid system is derived from a mixture of flow-dependent and

[1] The domain sizes of data assimilation are expanded to 28° × 28° for ghost d02 and 15° × 15° for ghost d03, respectively.

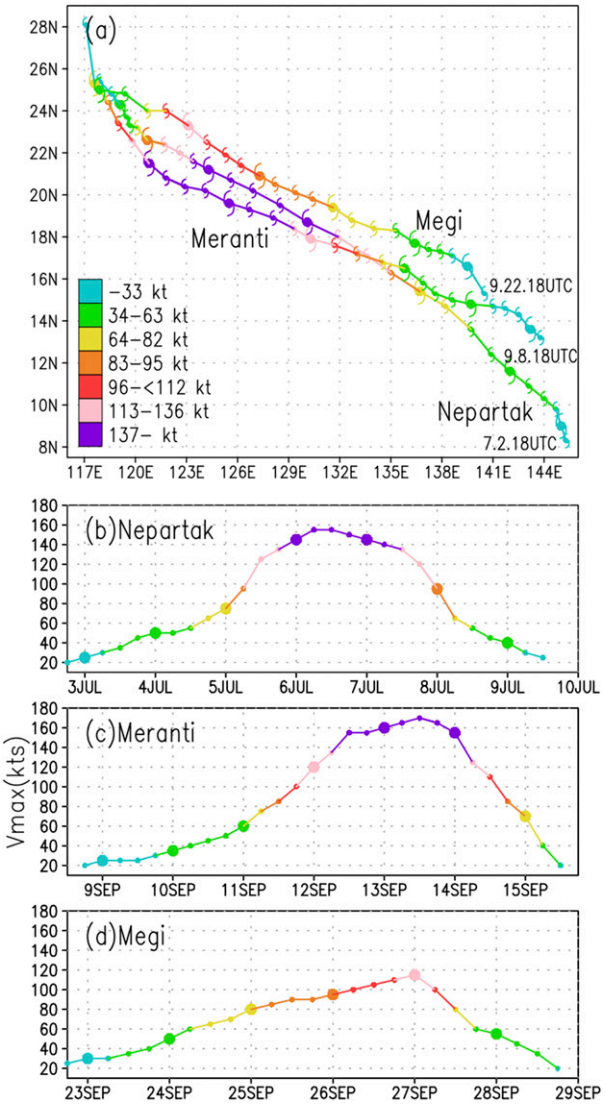

FIG. 1. (a) Track and (b)–(d) intensity of three TCs chosen in this study: (b) Nepartak, (c) Meranti, and (d) Megi in 2016. Each line color indicates storm intensity categories on the Saffir–Simpson hurricane wind scale.

static sources. The flow-dependent covariance is estimated from the GEFS 80-member ensemble or an HWRF 40-member ensemble. On the other hand, climatological (static) covariance is obtained through the National Meteorological Center (now NCEP) method (Parrish and Derber 1992; Wu et al. 2002). In the same fashion as the NATL and EPAC, the background error covariance composed from a linear combination is 80% flow-dependent (ensemble) and of 20% of static. The ensemble forecasts of HWRF are initialized or warm-started from the GEFS at each cycle in this study. All the experiments conducted utilize GSI quality control with default for the AMV dataset such as gross error check and height range check. No thinning and superobbing were done for the experiments with either OPAMV or H8AMV. Other than the AMV dataset, HWRF assimilates conventional observations (radiosondes, aircraft reports, ship, surface observations and so on) and satellite radiances (SSMIS, MHS, AMSU-A, and IASI). For those data, the default thinning was applied in the GSI. GSI default quality control for observations is applied to all experiments same as the AMVs.

TABLE 1. The start and end date of each case used in the experiment.

Case	Cycle period	No. of cycles
Nepartak	1800 UTC 2 Jul–0000 UTC 9 Jul 2016	26
Meranti	1200 UTC 8 Sep–1800 UTC 14 Sep 2016	26
Megi	0600 UTC 23 Sep–0600 UTC 28 Sep 2016	21

Data assimilation in HWRF is conducted in 6-h cycles, although the AMV datasets are derived at an interval of 1 h for OPAMV and 30 min for H8AMV. The first guess at appropriate time (FGAT) is used in HWRF to allow data within the 6-h time window (3-h from analysis time) to be properly assimilated. In FGAT, observations are compared with the first guess at the observation time, which is obtained by interpolating the two closest background fields in time within GSI. In this study, first guess are created at three time levels (3-, 6-, and 9-h forecast).

HWRF uses a process referred to as blending to avoid spindown of strong storms (Biswas et al. 2018; Tong et al. 2018; Pu et al. 2016). In the blending process, data assimilation increments are eliminated within a radius of 150 km from the TC center and below 600 hPa in the vertical. The increments are gradually reintroduced between 150 and 300 km in the radial direction and between 400 and 600 hPa in the vertical. The blending is used when the maximum sustained wind speed ≥65 kt (1 kt ≈ 0.5144 m s^{-1}). Even when the blending is turned on, full increments within 300 km radius are allowed in the upper levels, which is where the majority of our data exists. The impact is propagated to the inner core region

TABLE 2. Outline of HWRF experiments.

	Assimilation method	AMV assimilated
DAg	GEFS covariance	OPAMV within 1 h from the analysis time
DAgAMV	GEFS covariance	H8AMV from 3 h prior to 1 h after the analysis time
DAh	HWRF covariance	OPAMV within 1 h from the analysis time, same as DAg
DAhAMV	HWRF covariance	H8AMV from 3 h prior to 1 h after the analysis time, same as DAgAMV

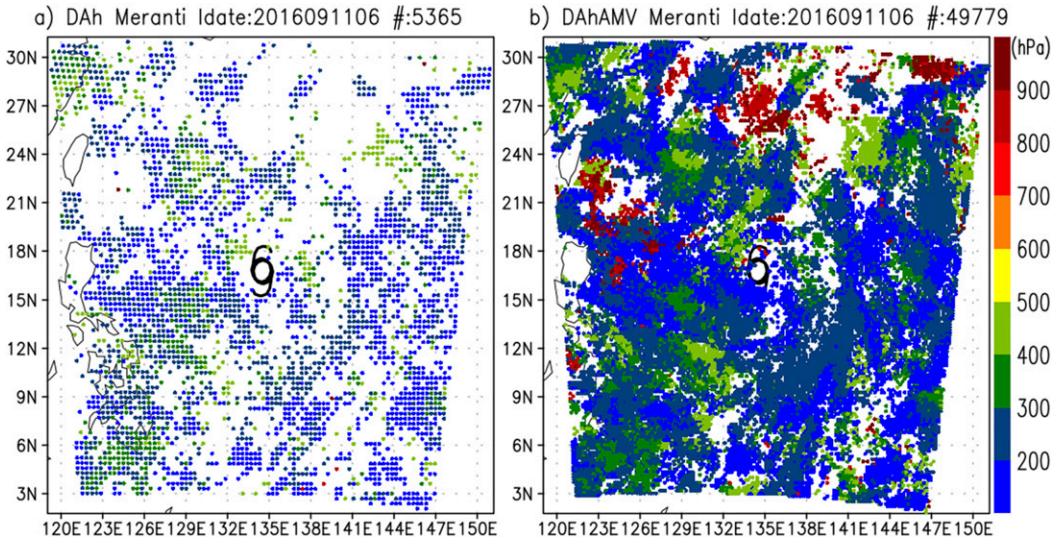

FIG. 2. Example of (high resolution) *Himawari-8* AMVs derived from the IR channel that were assimilated into the d02 of HWRF for the Meranti case in (a) DAh, and (b) DAhAMV experiments. Symbols plotted at the center of each panel indicate the TC center.

during 6-h forecast, which is utilized in the vortex initialization. The impacts of AMV assimilation is inherited through vortex-scale DA cycle.

c. *Cases of TCs*

To examine the impact of H8AMV, three TCs over the WPAC in 2016 are selected with a consideration of the forecast difficulty with respect to both track and intensity. Figure 1 shows the track and intensity of the three selected TCs: Nepartak (2016), Meranti (2016), and Megi (2016). The track and intensity data were obtained from the Joint Typhoon Warning Center (JTWC) best track. The start and end date for each TC when HWRF was run and the number of cycles are listed in Table 1.

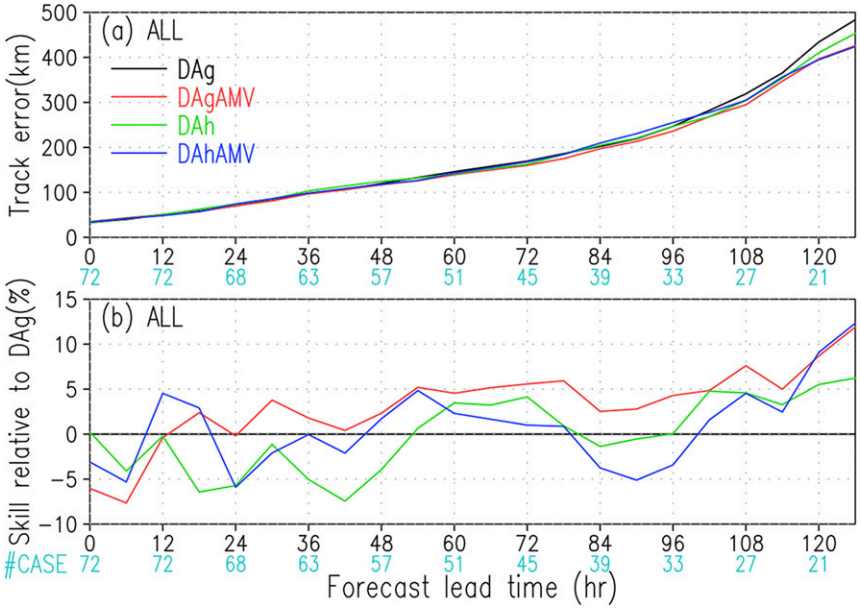

FIG. 3. Statistics of (a) track error with reference to the best track data and (b) track forecast skill relative to DAg for all cases. Numbers in cyan indicate sample size for each forecast lead time.

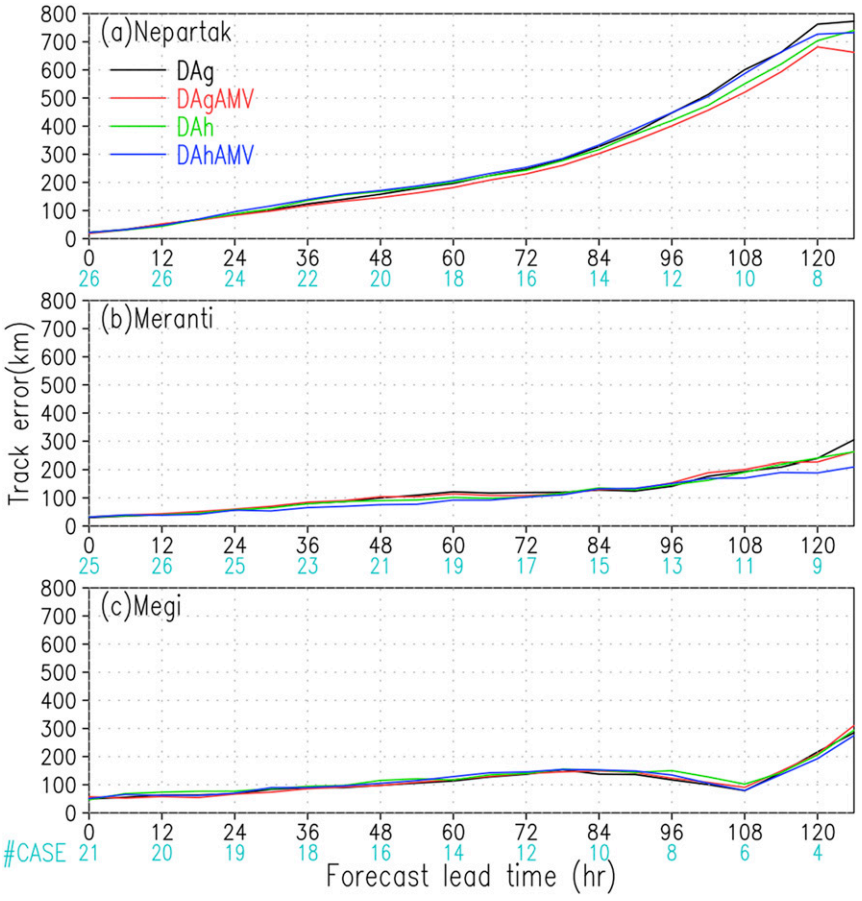

FIG. 4. Statistics of track error with reference to the best track data for (a) Nepartak, (b) Meranti, and (c) Megi in 2016. Numbers in cyan indicate sample size for each forecast lead time.

All three TCs have similar tracks, forming as a tropical depression near the island of Guam and moving to the west-northwest, passing near or over Taiwan, and making landfall in southeast China. However, the track errors forecasted by JMA-GSM (RSMC Tokyo-Typhoon Center 2016) were different among the three; the largest track error at 78 h was for Nepartak (333.3 km), followed by Meranti (266.5 km), then Megi (136.0 km).

The maximum sustained wind speed (Vmax) of Nepartak and Meranti reached 155 and 170 kt, respectively, corresponding to category 5 hurricane intensity. Both Nepartak and Meranti experienced extreme RI, with intensification rates of 70 kt day^{-1}. The Vmax of Megi was 120 kt, and the maximum intensification rate was 30 kt day^{-1}.

d. Experimental design

To investigate the impacts of H8AMV on the TC forecast in HWRF, four sets of experiments have been conducted, as shown in Table 2. The initial condition of the DAg experiment is obtained from the assimilation of conventional (including OPAMV) and satellite radiances observation data using the GSI ensemble–variational hybrid assimilation method with vortex initialization. The OPAMV was used within one hour of the analysis time. In the DAgAMV experiment, the forecasts are initialized from the assimilation of observation data used in the DAg experiment and from H8AMV. Note that the OPAMV used in the DAg experiment was first removed from the observation dataset before H8AMV was added to the dataset. In the DAgAMV experiment, the initial condition is the same as in the DAg, except that the H8AMV was ingested from three hours prior to one hour after the analysis time. The asymmetric assimilation window was used to make use of observation data as much as possible within a constraint of cutoff time. In this regard, the impacts would arise from not only the high spatiotemporal resolution but also the larger amount of AMV data. The total number of forecast cycles of the three TCs was 73 in each experiment. Examples of AMVs

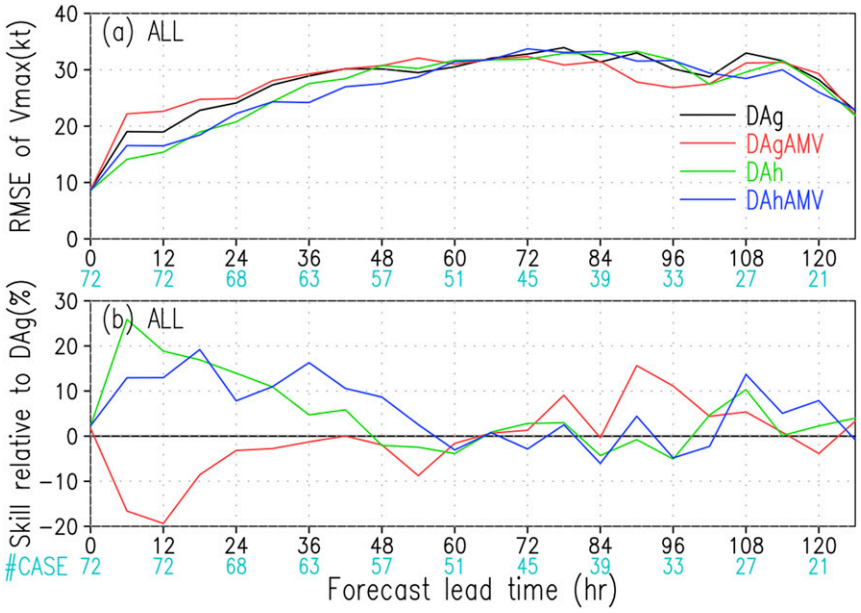

FIG. 5. As in Fig. 3, but for RMSE and skill of Vmax.

assimilated into the HWRF outer nested domain are shown in Fig. 2. In this case, the number of AMV observations assimilated into the d02 of HWRF are 5365, and 49779 in the DAh, and DAhAMV, respectively. The AMV data rejected by quality control in this experiment was 10–20%.

To explore ways of making more effective use of H8AMV by changing the background error covariance in GSI, two additional sets of experiments have been performed. The DAh experiment used the HWRF 40-ensemble members instead of GEFS 80-ensemble members as the background error covariance. In the DAhAMV experiment, the observation data used for creating the initial condition is the same as the DAgAMV experiment, except for the use of the background error covariance created from HWRF ensemble members. The list of experiments is summarized in Table 2.

3. Numerical results

In this section, verification results for track, intensity, and size are described. The skill or improvement rate relative to DAg is defined by

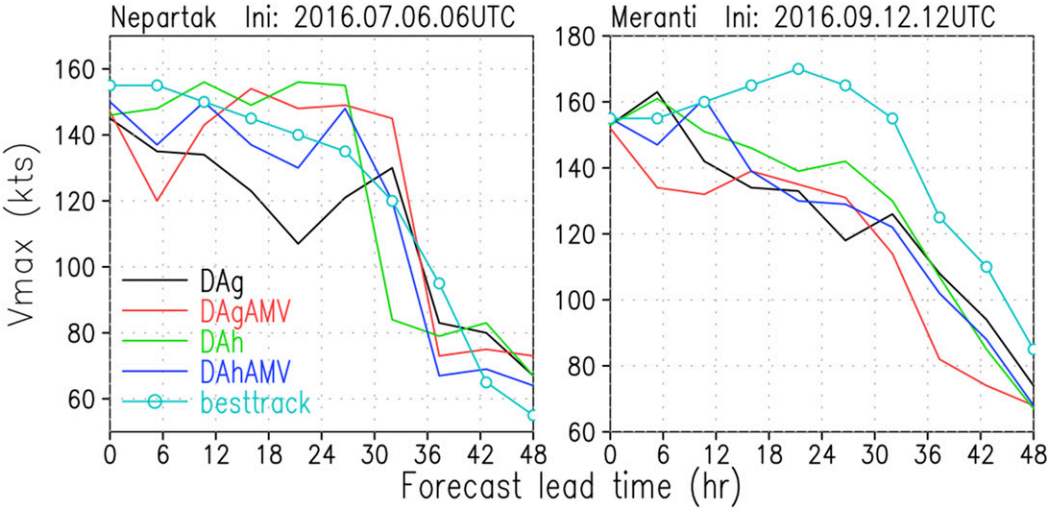

FIG. 6. Time series of Vmax (left) for Nepartak and (right) for Meranti.

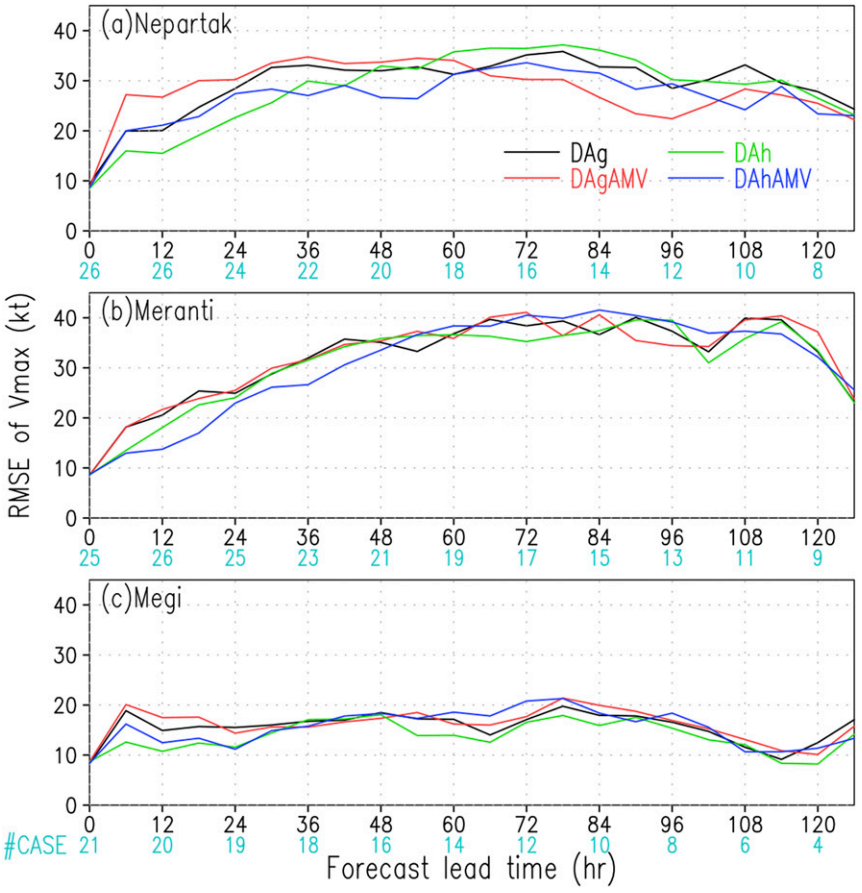

FIG. 7. As in Fig. 4, but for RMSE of Vmax.

$$\text{Skill} = 100(E_{\text{DAg}} - E_{\text{model}})/E_{\text{DAg}}, \quad (1)$$

where E_{DAg} and E_{model} are the mean track error or root-mean-square error (RMSE) of intensity or size from DAg and a given model, respectively. Note that there are few statistical significance at the 95% level for the verification using paired t test between DAg and each experiment, especially for each case because of the limitation of sample size.

a. Track forecast

The track forecast verification for all three TCs (Fig. 3) shows that DAgAMV is the best for forecast lead times (FT) of 30–114 h (FT = 30–114 h) in the four experiments, followed by DAh and DAhAMV. The improvement rate of DAgAMV with respect to the DAg ranges from 4% to 12% beyond FT = 54 h except FT = 84–90 h. It indicates that assimilating H8AMV with GEFS covariance improves the track forecast skill. On the other hand, the improvement rate of DAhAMV is smaller than that of DAgAMV at most forecast lead times. There is little net benefit of using HWRF covariance for track forecast when H8AMV is used in this configuration and in this case at least. This result implies that HWRF covariance is suboptimal for the larger scales that control the track.

The improvement in track forecast skill at longer forecast lead times is different from the result shown by Velden et al. (2017), which showed degradation at the longer forecast lead times (>FT = 96 h). This difference could arise from several factors such as the different assimilation scheme, size of assimilation domain, observation data, model setup, and cases in a different basin. While understanding the cause of the skill difference is important, it is beyond the scope of this study.

To examine the case dependency, track verification for each TC is shown in Figs. 4a–c. The result clearly shows there is case to case variability; assimilating H8AMV (DAgAMV) shows an improvement for Nepartak and is neutral for Meranti and Megi with regard to the DAg. On the other hand, DAhAMV shows an improvement for Meranti and is neutral for Nepartak and Megi with regard to the DAg. Note that the track forecast errors for Meranti and Megi in the DAg were considered quite

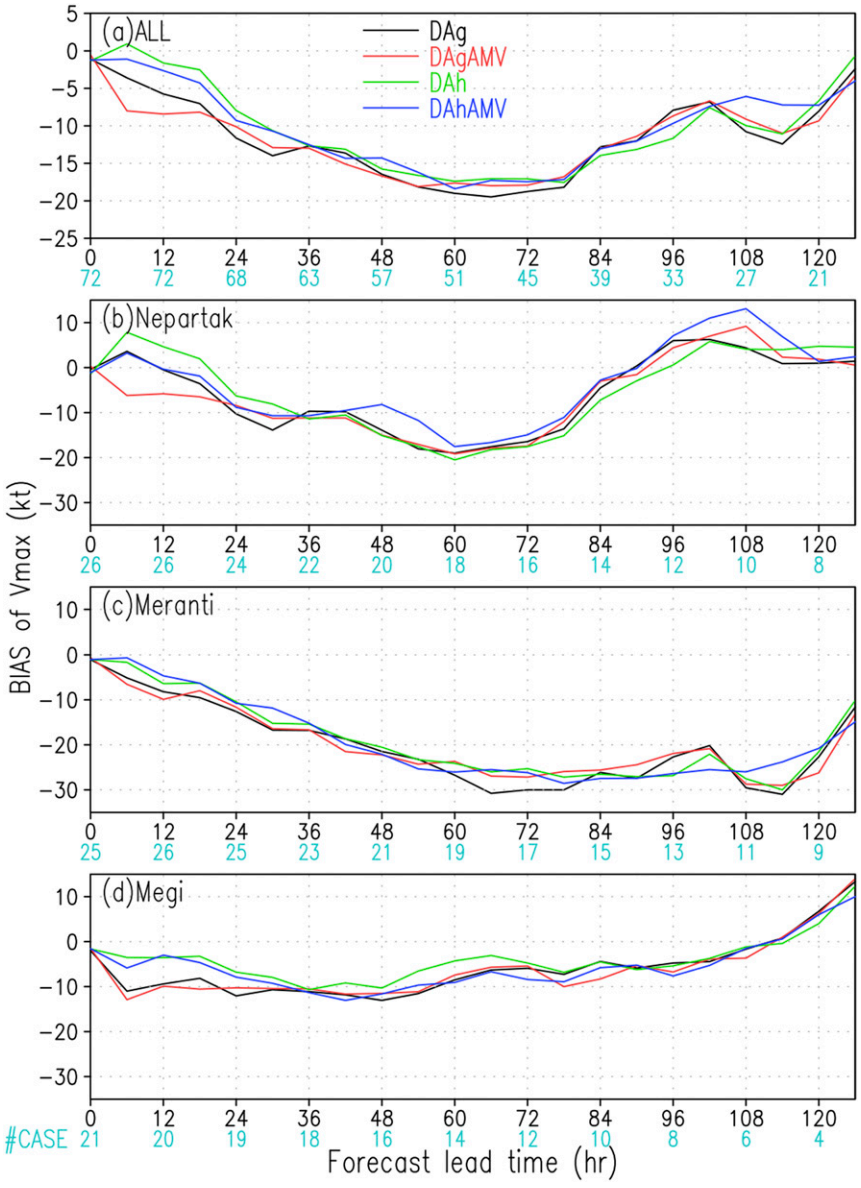

FIG. 8. As in Fig. 4, but for bias of Vmax with reference to the best track data.

low. In other words, the track errors are below the average of the official track forecast errors (243, 316, and 442 km at FT = 3, 4, and 5 days) for 2016 WPAC TCs (RSMC Tokyo-Typhoon Center 2016). The small track error implies that the environmental flow is well represented so that the assimilation has less room for impact.

b. *Intensity forecast*

The intensity forecast is verified for maximum sustained surface winds or Vmax in this study. Figure 5 shows the RMSE of Vmax for all cases, and the intensity error (RMSE of Vmax) with DAgAMV is the largest for shorter forecast lead times (FT = 6–54 h). The intensity error is larger in DAhAMV than DAh up to FT = 12 h, meaning that the H8AMV assimilation using HWRF covariance still shows the degradation of intensity forecast skill for shorter forecast lead time compared to the OPAMV assimilation.

The intensity degradation is mainly caused by spindown, which occurs for strong storms, as remarked by Tong et al. (2018) and Lu et al. (2017b). Figure 6 shows the time evolutions of Vmax as an example of spindown for Nepartak and Meranti case. The forecast lead time of up to 48 h is shown to focus on the initial forecast. The intensity in both DAgAMV and DAhAMV weakens by 10–20 kt during the first 6 h. Compared to the experiments

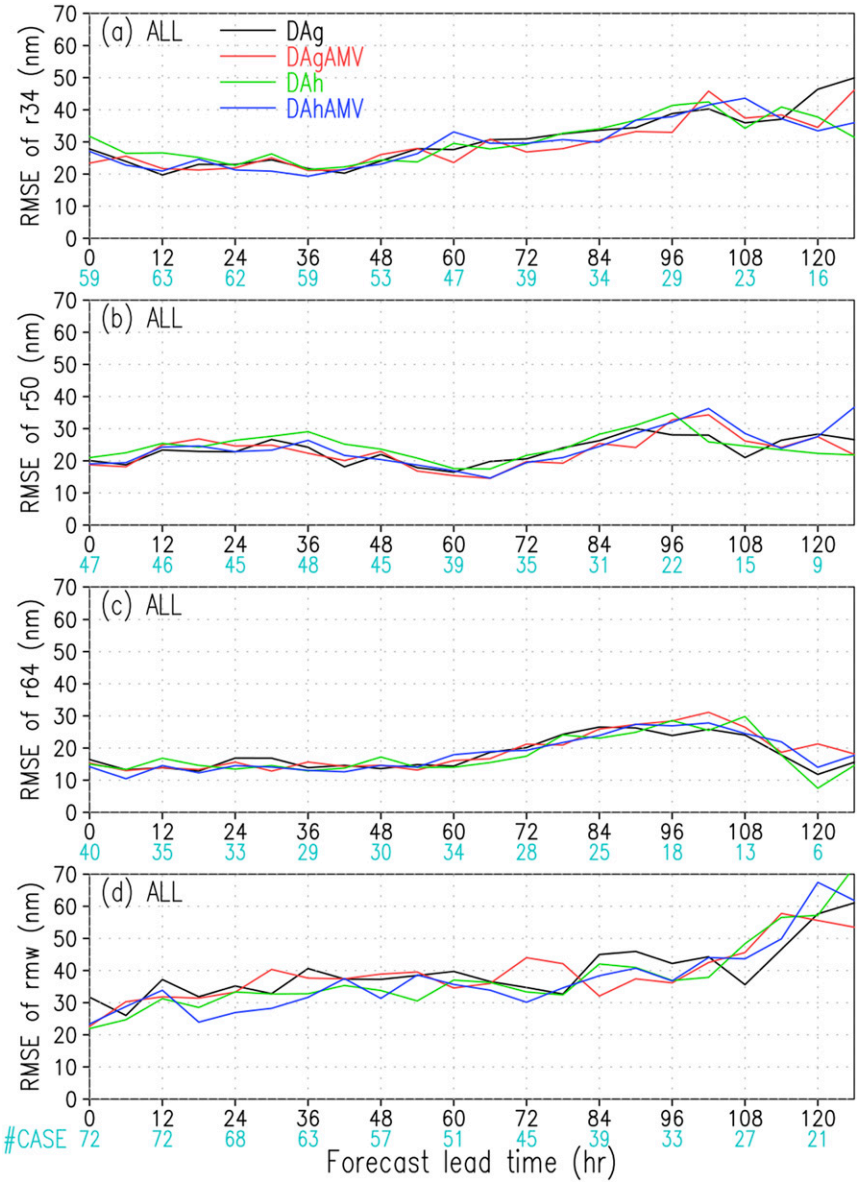

FIG. 9. Statistics of RMSE of TC size with reference to the best track data for all cases. (a) R34, (b) R50, (c) R64, and (d) RMW. Numbers in cyan indicate sample size for each forecast lead time.

adding the H8AMV, the Vmax drop in DAg and DAh is small or does not occur. The assimilation of inner-core reconnaissance observation for strong storms leads to spindown because of the suboptimal error covariance (Lu et al. 2017b) and the interaction between model bias and VI (Tong et al. 2018). The similar spindown occurs when the H8AMV is assimilated because there is much more H8AMV data than OPAMV data close to the inner core (Fig. 2). Note that spindown only impact the Vmax skill up to 36 h (Fig. 5b) and there is some improvement for longer lead time, consistent with Tong et al. (2018).

Case-to-case variability in intensity can be found in the similar way as the track forecast for longer forecast lead times in Fig. 7. The intensity error in DAhAMV was larger than that in DAh at FT = 6–30 h for Nepartak (Fig. 7a), although it was smaller for Meranti (Fig. 7b).

For the intensity bias for all cases (Fig. 8a), DAg and DAgAMV have negative (weak) intensity bias mainly because of the spindown issue (e.g., Fig. 6), especially of Nepartak (Fig. 8b) and Meranti (Fig. 8c). For Meranti, the weak intensity bias for all experiments reached larger than 25 kt, which was 5–20 kt larger

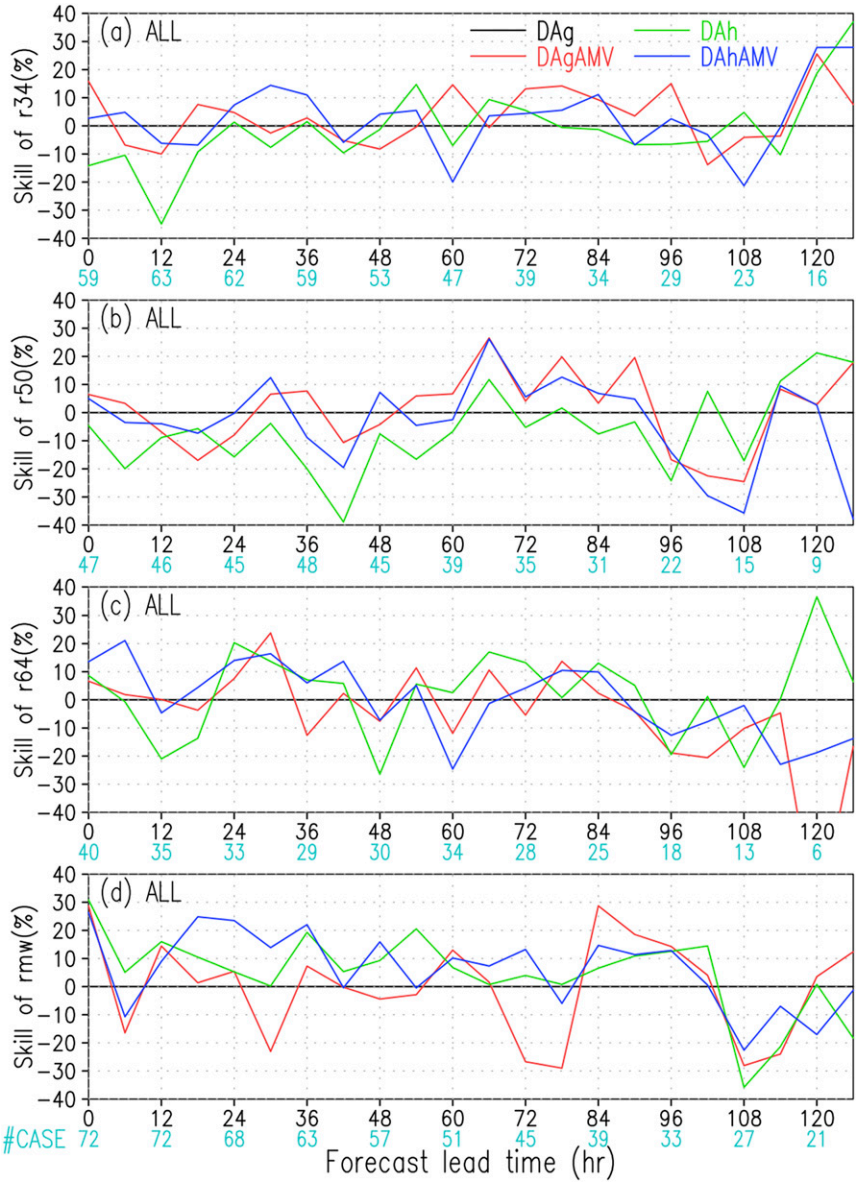

FIG. 10. As in Fig. 9, but for size forecast skill relative to DAg.

than those for Nepartak and Megi. Consistent with the intensity error, the intensity bias with DAgAMV was the larger than those with DAg for shorter forecast lead times. The weak intensity bias is consistent with Lim et al. (2019), which showed the HWRF had a weak bias for strong TCs. The impact on intensity bias was neutral for Megi, which was a weak bias of 5–10 kt in all experiments. The result indicates using the background covariance created from the HWRF ensemble effectively alleviates the intensity errors and biases due to spindown arising from using the covariance created from the GEFS ensemble for shorter forecast lead times and for all three TC cases. The result is consistent with the finding by Tong et al. (2018) and Lu et al. (2017b).

c. *Size forecast*

The RMSE of TC size (R34, R50, R64, and RMW) and its skill for all cases are shown in Figs. 9 and 10, respectively. For R34, R50, and R64, averages of the radii over four different quadrants were taken. A sample was included in this size verification if at least three of the quadrants have a value for the wind radius and this occurs in all four experiments, to homogenize the sample.

From Figs. 9 and 10, it is clear to see that RMW improvement mainly comes from HWRF covariance

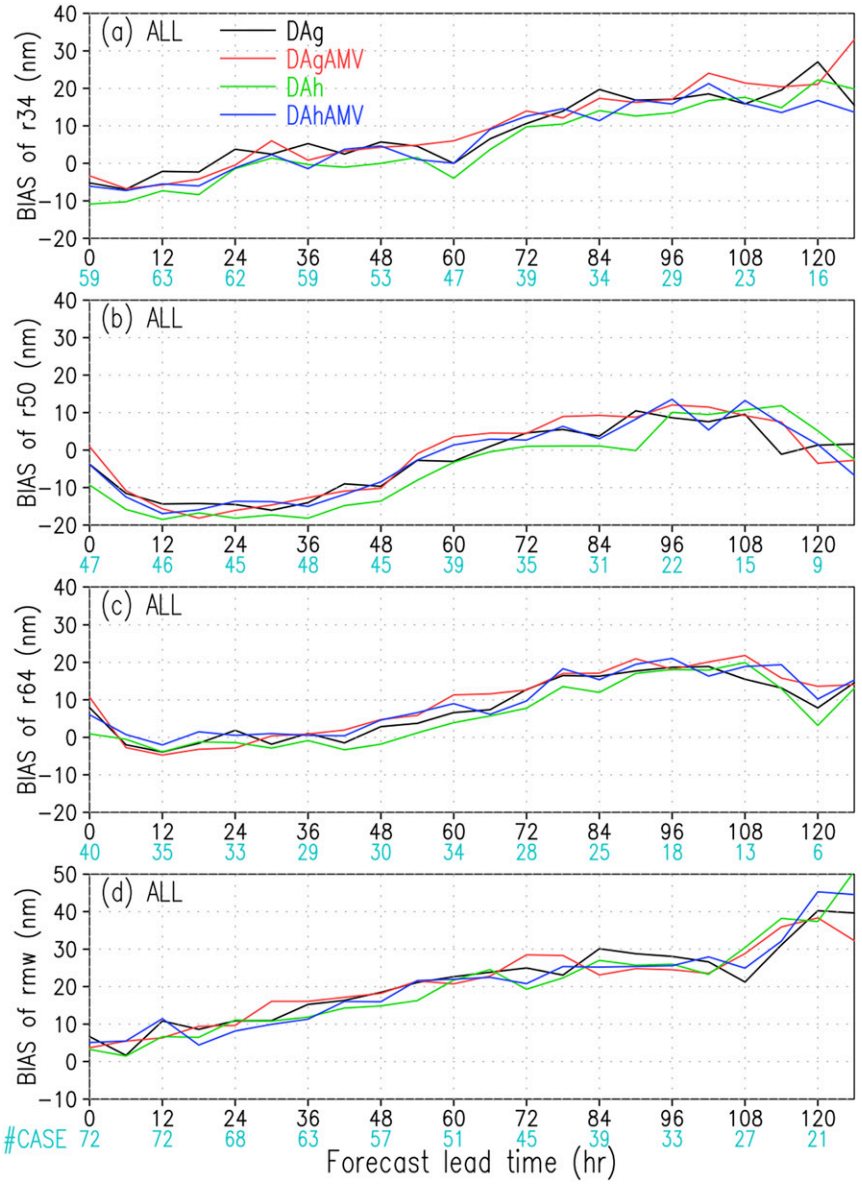

FIG. 11. As in Fig. 9, but for bias of TC size.

because both DAh and DAhAMV are better than DAg and DAgAMV, respectively. The improvement rate for RMW in DAh (DAhAMV) with respect to DAg (DAgAMV) reaches 9.7% (7.5%) on average for FT = 0–96. However, there was a degradation for R34 and R50 in DAh (DAhAMV) with respect to DAg (DAgAMV), although the impacts are neutral for R64 in DAh (DAhAMV) with respect to DAg (DAgAMV). Furthermore, for R34 and R50 improvement, the contributions are mainly from H8AMV data because DAgAMV and DAhAMV are better at more than half of forecast lead times than DAg and DAh, respectively. The addition of H8AMV contributes to a 3.9% (5.5%) and 2.7% (10.2%) improvements in R34 and R50, respectively, on average for FT = 0–96 in DAgAMV (DAhAMV) compared to DAg (DAh). This is consistent with the result documented by Lim et al. (2019), which remarked that an improvement was achieved when the hourly AMVs were assimilated. A combined impact of H8AMV and HWRF covariance shows that the improvement rate in DAhAMV with respect to DAg reaches 11.0% on average for FT = 0–96. The result highlights that there is a significant benefit of using the H8AMV with HWRF covariance in storm size forecast.

The verification of TC size biases shows DAh tends to reduce all the size metrics for forecast lead times of up to

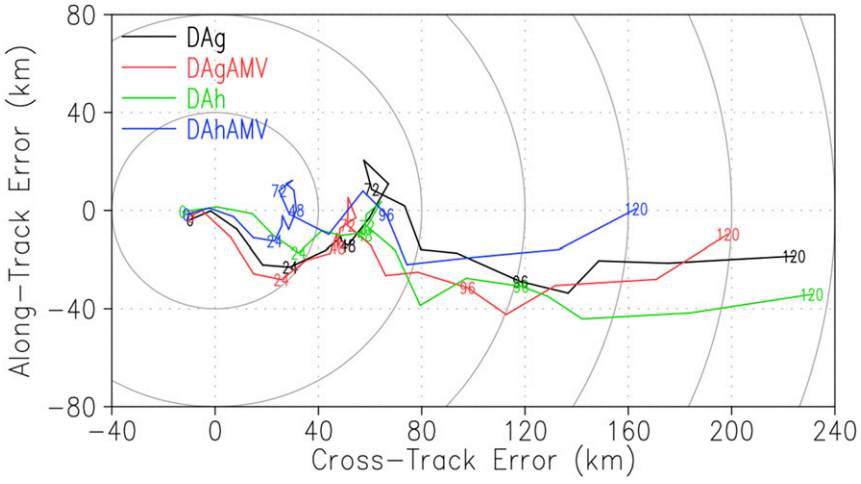

FIG. 12. Mean along- (*y* axis) and cross-track (*x* axis) errors at each forecast lead time and for each experiment. Each plot shows the track error averaged for Meranti case and for all forecast cycles. The positive value in the along-track error indicates the forecasted track is too fast, and the positive value of the cross-track error means the track is too far to the right. Numbers on each line indicate the forecast lead times.

FT = 96 h compared to DAg. R34 and R50 were smaller at more than half of forecast lead times in DAhAMV than in DAgAMV. HWRF covariance would play a part in reducing the TC size. The impact of TC size biases on H8AMV shows R34, R50, and R64 were larger in DAhAMV than DAh (Fig. 11). On the other hand, there was no systematic difference in all the size metrics between DAgAMV and DAg. The impact of adding H8AMV is not as obvious as that of HWRF covariance.

The biases of R34 and RMW increase with the forecast lead time in the all experiments, indicating a systematic bias in the HWRF physics because the increasing trend does not depend on the initial condition. It is worth mentioning that both the size error and bias seem to be small or comparable to R34, R50, and R64 in the previous version of HWRF (Tallapragada et al. 2015), despite the challenging cases selected. Note that the vortex structure is quite modulated by the vortex initialization, and an additional experiment which has no the vortex initialization would be needed to extract a clearer impact of the assimilation on TC size.

4. Further comparison and analysis

a. Diagnosis of track error difference

The track verification shows the inclusion of H8AMV has a positive impact on track forecast (Figs. 3 and 4). To assess the cause of the reduction in track forecast error, the track error is separated into along- and cross-track errors (Neumann and Pelissier 1981). The along-track error indicates whether the forecasted track is too fast (positive value) or slow (negative value), and the cross-track error shows whether the track is too far to the right (positive value) or left (negative value). Figure 12 displays the average along- and cross-track errors for Meranti for the all cycles in each experiment, which corresponds to the track error bias in the along- and cross-track directions. There is a pronounced bias to the right-of-track (positive cross-track error bias) in all the experiments and a rather slow track tendency for longer forecast lead time in all the experiments except DAhAMV. The right-of-track bias here is almost equivalent to a north-northeast bias in the geographical sense because Meranti tracked to the west-northwest (Fig. 1). A northward bias is found at several NWP centers in the previous study, especially east of the Philippines (Yamaguchi et al. 2012). The northward bias or cross-track error bias was smallest with DAhAMV, followed by DAgAMV. It shows the benefit from assimilating H8AMV on the track forecast.

TC motion is affected by both the steering flow surrounding the TC and the TC structure (size) through the beta gyre effect discussed in previous studies (Chan and Williams 1987; Fiorino and Elsberry 1989), and the assimilation of H8AMV could change both factors. To diagnose the factors for track error reduction from assimilating H8AMV, the optimal steering flow radius and depth are estimated according to Galarneau and Davis (2013). The steering flow was defined as the area- and vertically averaged environmental flow, once the cyclonic circulation associated with the TC was removed. The vertical extent of the steering layer ranged from 50 to 650 hPa, with a fixed base at 850 hPa, using eight different radii ranging from 100 to 800 km from the TC

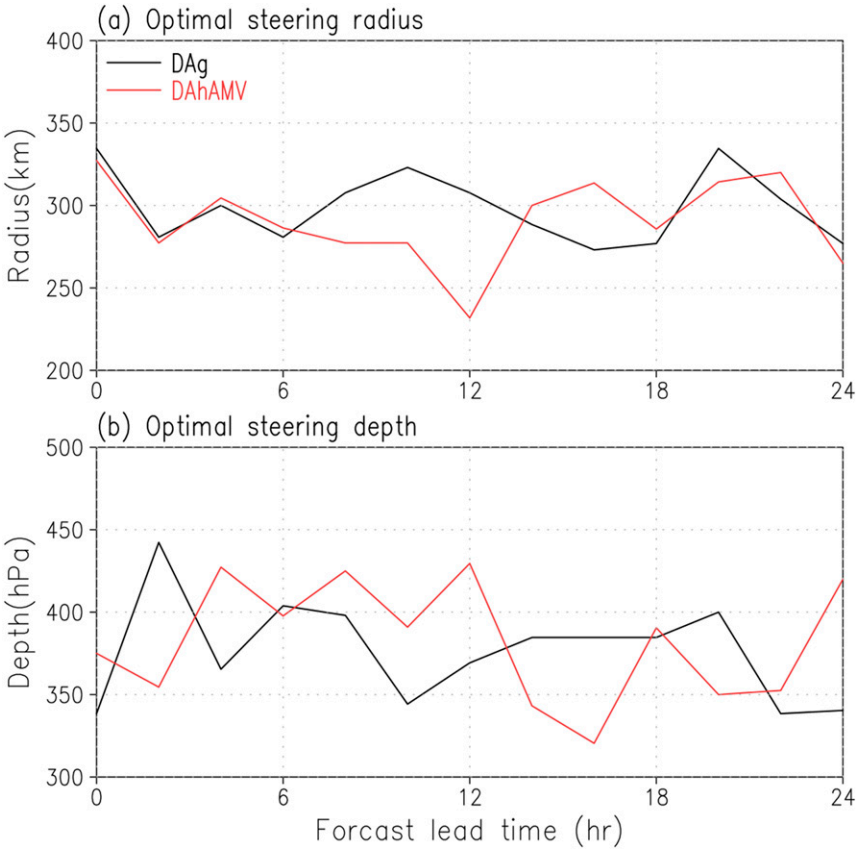

FIG. 13. (a) Radius and (b) depth of the optimal steering flow for the Meranti case. Values are averaged for 26 cycles.

center. The radius and depth combination that produces the smallest vector difference between the averaged steering flow and the actual track motion is chosen as the optimal steering flow radius and layer at a given time. The differences in either optimal steering flow radius (size) or height could be identified if the assimilation impacts the TC structure. Otherwise, the small steering flow differences caused by the assimilation at initial time put TCs on different trajectories. Here, the difference between DAg and DAhAMV for Meranti is analyzed because the difference between the two was the largest.

The estimated optimal steering flow radius and depth (Fig. 13) are similar in DAg and DAhAMV. The optimal steering radii (depths) averaged for 0–24 h are 299 km (376 hPa) and 289 km (386 hPa) in DAg and DAhAMV, respectively. The small differences in the optimal steering flow radius between DAg and DAhAMV are consistent with the size bias in Fig. 11, which shows there is no significant difference between the two.

To examine the steering flow difference between the two as a factor for the track error difference, the time evolution of the steering flow profile difference is calculated (Fig. 14). The steering flow is defined using a radius of 300 km from the TC center for the two experiments. The value of 300 km was chosen from the average optimal steering radius. The arrows display the steering flow difference between DAhAMV and DAg (DAhAMV minus DAg). If the steering flow difference arises from the TC size difference through the beta gyre effect, the persistent meridional flow difference could be identified at the early forecast lead times. After FT = 24 h or so, the dominant signal of steering flow difference comes from the TC location biases so that the first 24 h is examined.

The differences in initial steering flow between DAhAMV and DAg are consistent with the differences in track biases (Fig. 12). The easterly component is relatively larger at the middle troposphere (550–350 hPa) for the first 9 h in DAhAMV. The larger easterly component alleviates the slow track bias for the early forecast lead times. There is little persistent meridional flow during FT = 0–24 except at 500 hPa, indicating that the steering flow difference arising from TC size difference is negligibly small. Thus, the difference in track forecast errors between DAg and DAhAMV seems to be attributed to the initial steering flow difference, not to the TC size difference.

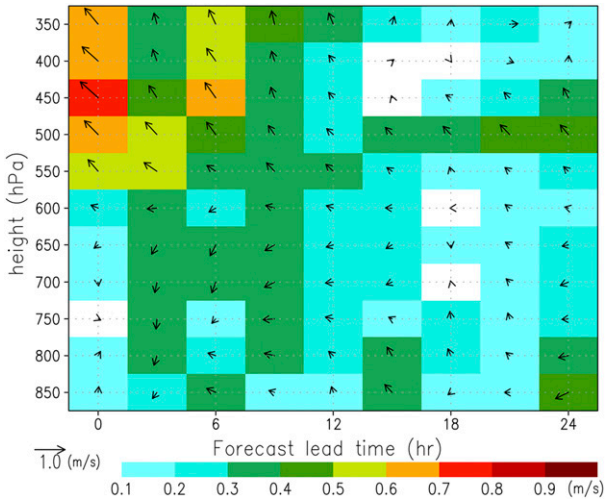

FIG. 14. Time–height cross section of steering flow differences between DAhAMV and the DAg (DAhAMV minus DAg). The differences are averaged over 26 cycles for the Meranti case. The *x* axis is forecast lead time. An arrow displays difference in the areal average of steering vectors within the 300-km radius from the TC center at each forecast lead time. Color displays magnitude of difference in steering vectors.

b. Factors impacting intensity bias

The intensity bias and error for Meranti case were the largest with DAgAMV, as shown in Figs. 8c and 7b, although there are the same track biases among the experiments at shorter lead times (Fig. 12). The result indicates the intensity error originates from the inner core dynamics, not from the environmental factors. To investigate the cause of the significant weak bias for Meranti in DAgAMV, the vertical structure of azimuthally averaged tangential wind speeds for all experiments are compared (Fig. 15). The analysis was conducted by interpolating the HWRF output on pressure coordinates to the height coordinate. The radial structure is normalized by the radius of maximum azimuthally averaged wind at 2-km altitude based on a previous study (Rogers et al. 2013) to highlight the difference in essential TC structure, which is not associated with RMW difference between each experiment and DAg. The composite is produced by averaging 18 cycles from cycle 3 to cycle 20, corresponding to Meranti's intensification through to the mature stage. The averaged RMWs at 2-km altitude were 59.6, 53.5, 60.3, and 63.8 km in DAg, DAgAMV, DAh, and DAhAMV, respectively.

Assimilating H8AMV with GEFS covariance generates stronger vortices outside the RMW at the lower troposphere (Fig. 15b). This pattern corresponds to the enhancement of inertial stability outside the RMW, which would reduce the low-level inflow because of high resistance to radial displacement. In DAhAMV, the low-level tangential flow is not significantly impacted. Instead, the tangential wind near and outside the RMW is enhanced above the middle troposphere (above 5-km height) compared to DAgAMV. This corresponds with a taller vortex, which favors intensification.

The radial wind differences, averaged for FT = 0–12 h between each experiment and DAg for the lower troposphere (Fig. 16), show a substantial weakening of the low-level inflow in DAgAMV. The maximum inflow speeds in the boundary layer are 10.5, 9.7, 12.2, and 12.9 $m\,s^{-1}$ in DAg, DAgAMV, DAh, and DAhAMV, respectively. The inflows are stronger in DAh and DAhAMV than in DAg and DAgAMV. The weakening of inflow bring slower intensification due to lower angular momentum transport in DAgAMV. This is consistent with the observational study by Rogers et al. (2013). They showed that the composite of axisymmetric tangential wind for intensifying TCs was weaker outside the RMW than that for steady-state TCs.

The previous studies using numerical simulations pointed out that TCs with larger intensification had a strong inflow (Gopalakrishnan et al. 2013; Kanada and Wada 2015; Chang and Wu 2017), which also supports the results of this study. The assimilation of H8AMV using GEFS covariance could degrade the inner core of the TC, leading to a slower intensification, even though VI is applied as found by Tong et al. (2018). This degradation of inner core dynamical structure or spindown issue can be avoidable by applying the covariance created from the HWRF ensemble.

Several previous studies pointed out that the RI tends to occur when the flow structure becomes more axisymmetric (Miyamoto and Takemi 2013, 2015; Miyamoto and Nolan 2018), and the storm tends to intensify more rapidly when the storm structure becomes more axisymmetric (Shimada et al. 2017). From this viewpoint, the axisymmetricity is calculated from the potential vorticity as defined by Miyamoto and Takemi (2013). The areal averaged values of axisymmetricity within the RMW at 2-km altitude and for z = 2–8 km are 0.86, 0.84, 0.88, and 0.81 in DAg, DAgAMV, DAh, and DAhAMV, respectively. The differences in axisymmetricity among the experiments seem to be too small to account for the different intensification rate (not shown).

The importance of initial inner-core moisture in the TC intensity forecast was found by Emanuel and Zhang (2017). The inner core region in their study was defined as a region within 300-km radius from the TC center. A comparison of azimuthally averaged relative humidity (Fig. 17) shows the initial vortices become moister around and outside the RMW at the middle troposphere and become drier inside the RMW above 5-km height in DAh and DAhAMV than in DAg and DAgAMV.

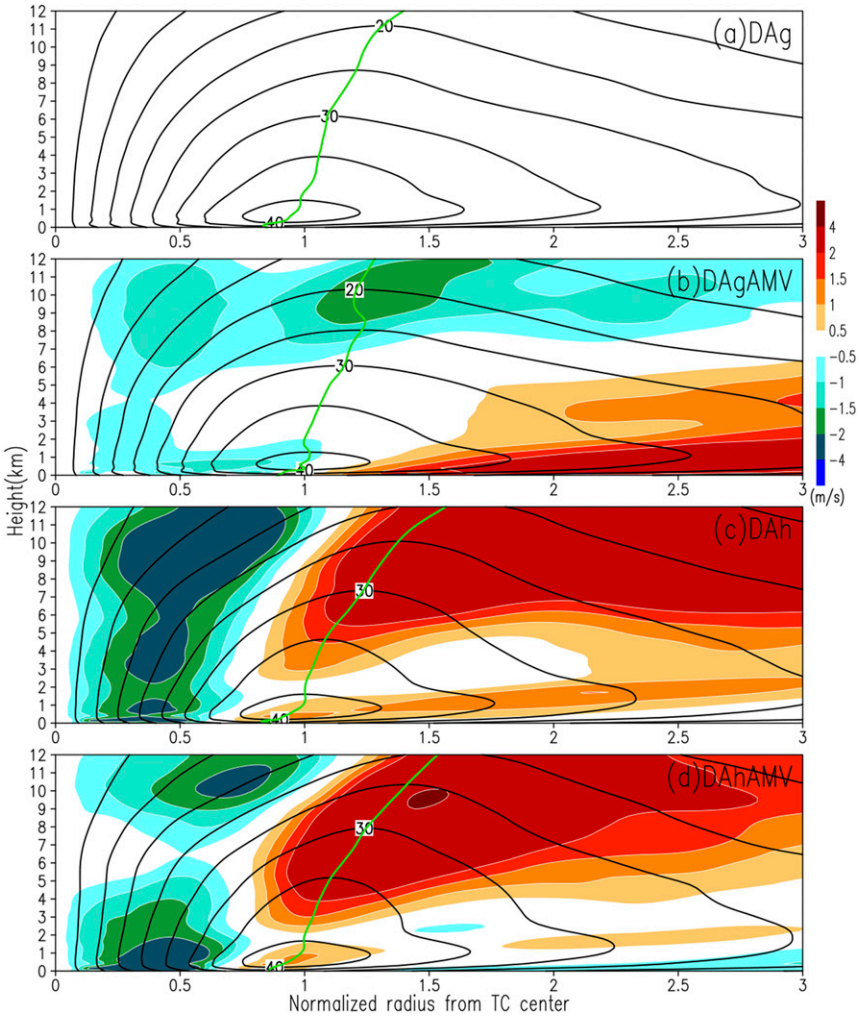

FIG. 15. Radial–height cross section of azimuthally averaged tangential wind for Meranti. A contour displays azimuthally averaged tangential wind. Color shading displays the difference in azimuthally averaged tangential wind (each experiment minus DAg). Green thick line indicates the radius of maximum wind (RMW) at each height level.

The drier air in DAh and DAhAMV is well inside the RMW, which is consistent with the pattern of strong or intensifying TC, and also consistent with the stronger vortices aloft. The moistening around and outside the RMW when HWRF covariance is used seems to increase the intensification rate. The background error covariance generated from HWRF ensemble provide not only the flow-dependent features but also cross-variable correlations in the TC inner core more reasonably than the background error covariance generated from GEFS ensemble, as found by Lu et al. (2017a).

The upper-level warm core is also considered to relate to the intensification (Zhang and Chen 2012; Chen and Zhang 2013). The maximum temperature deviations, which are defined as the temperature anomaly from the mean temperature averaged over 550–650 km from the TC center at the upper-level core, are between 9.1 and 10.0 K in all the experiments, and whose differences in the two experiments are less than one degree. The initial warm cores were not significantly different from each other (not shown).

5. Summary and discussion

We investigate the impact of assimilation of high-resolution AMVs derived from the full disk scan of the new generation geostationary satellite *Himawari-8* (H8AMV) on TC forecasts in the western North Pacific basin. Forecast experiments for three TCs in 2016 are performed using GSI-based ensemble–variational hybrid DA with HWRF. The results show that the inclusion of H8AMV with GEFS covariance can benefit the

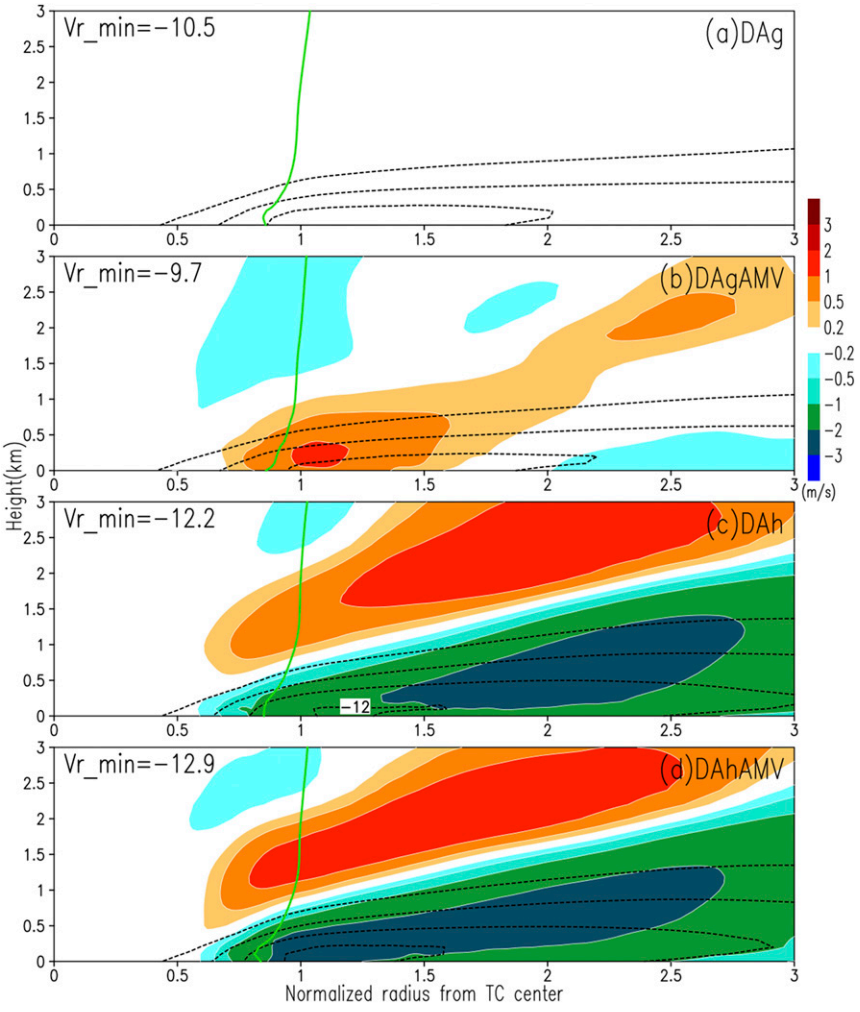

FIG. 16. As in Fig. 15, but for azimuthally and temporally averaged radial wind. Color shading displays the difference in azimuthally radial wind averaged for 0–12 h (each experiment minus DAg). A dashed contour displays negative radial wind or inflow. Contour interval is 2 m s^{-1}.

track forecast skill, especially for long-range lead times (beyond 54 h). The optimal steering flow diagnosis indicates that the improved track forecast here seems to be attributed to an improvement in the initial steering flow surrounding the TC, not in the representation of TC structure, such as its size and depth.

The assimilation of H8AMV with GEFS covariance, however, increases the negative intensity bias and intensity error, especially for short-range lead times (~24 h). This is caused by spindown reported by Tong et al. (2018) and Pu et al. (2016). The investigation of structural changes from the assimilation of H8AMV revealed the following two factors that are likely to relate to this degradation: 1) an increase of tangential wind speed (inertial stability) outside the RMW, resulting in a weakening of the boundary layer inflow; and 2) a drying around and outside the RMW. By assimilating H8AMV using HWRF covariance, the negative intensity bias was significantly alleviated and there is a significant improvement in size forecast skill. Consistent with Lu et al. (2017b), the intensity bias was improved through the proper representation of TC inner core structure by using the flow-dependent estimate of the background error covariance created from HWRF ensemble, not GEFS ensemble.

Although there are promising results in this study, several caveats exist as well. There is little benefit of assimilating H8AMV for track forecast when HWRF covariance is used. The low benefit implies HWRF covariance is suboptimal for the larger scales that control the track. Several recent studies showed that hourly assimilation cycles (Lu et al. 2017a) and 10-min assimilation cycles (Honda et al. 2018) have a potential to improve the TC forecast, while this study used 6-h DA cycles.

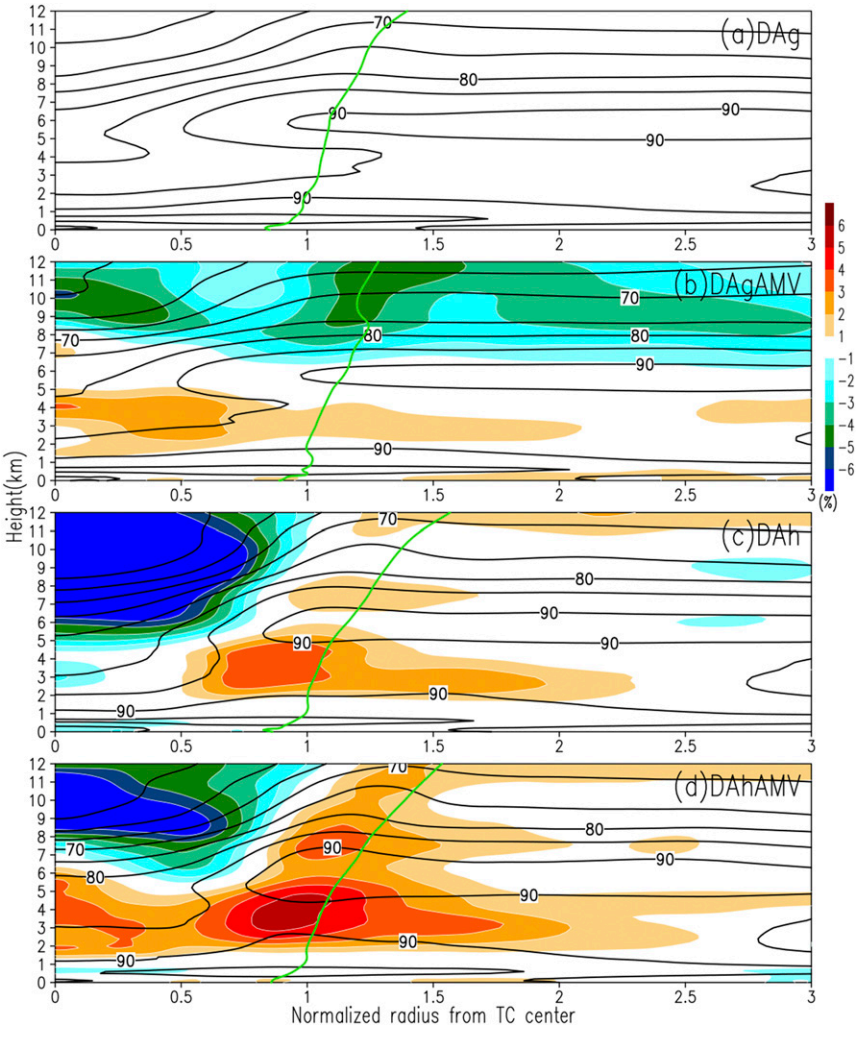

FIG. 17. As in Fig. 15, but for azimuthally averaged relative humidity. A contour displays azimuthally averaged relative humidity in each experiment. Contour interval is 5%.

The assimilation of higher temporal and spatial resolution AMVs derived from the regional scan of *Himawari-8* or rapid-scan AMVs, which improved the forecast of precipitation events (Kunii et al. 2016), might provide a better representation of TC structure and the surrounding area, leading to an improvement in forecast skill. These are reserved for a future study.

Acknowledgments. The authors appreciate valuable comments by Dr. Jason Sippel and two reviewers and it was of great help for improving the manuscript. The experiments are performed on the NOAA RDHPCS supercomputer Theia. Some results and descriptions were included in the abstract of the authors' AMS conference presentation, and in progress reports to NSF. This work was supported by NOAA's Hurricane Forecast Improvement Project (HFIP) and NOAA's Next Generation Global Prediction System (NGGPS) program. This work was also supported by Ministry of Education, Culture, Sports, Science and Technology (MEXT) KAKENHI Grant 16K05556. We thank Ms. Mary Hart for her assistance in carefully proofreading this manuscript.

REFERENCES

Aberson, S. D., and J. L. Franklin, 1999: Impact on hurricane track and intensity forecasts of GPS dropwindsonde observations from the first-season flights of the NOAA Gulfstream-IV Jet Aircraft. *Bull. Amer. Meteor. Soc.*, **80**, 421–427, https://doi.org/10.1175/1520-0477(1999)080<0421:IOHTAI>2.0.CO;2.

——, A. Aksoy, K. J. Sellwood, T. Vukicevic, and X. Zhang, 2015: Assimilation of high-resolution tropical cyclone observations with an ensemble Kalman filter using HEDAS: Evaluation of 2008–11 HWRF forecasts. *Mon. Wea. Rev.*, **143**, 511–523, https://doi.org/10.1175/MWR-D-14-00138.1.

Bessho, K., and Coauthors, 2016: An introduction to Himawari-8/9—Japan's new-generation geostationary meteorological satellites. *J. Meteor. Soc. Japan*, **94**, 151–183, https://doi.org/10.2151/jmsj.2016-009.

Biswas M. K., and Coauthors, 2018: Hurricane Weather Research and Forecasting (HWRF) Model: 2017 Scientific Documentation. NCAR Tech. Note NCAR/TN-544+STR, 111 pp., https://doi.org/10.5065/D6MK6BPR.

Chan, J. C., and R. T. Williams, 1987: Analytical and numerical studies of the beta-effect in tropical cyclone motion. Part I: Zero mean flow. *J. Atmos. Sci.*, **44**, 1257–1265, https://doi.org/10.1175/1520-0469(1987)044<1257:AANSOT>2.0.CO;2.

Chang, C., and C. Wu, 2017: On the processes leading to the rapid intensification of Typhoon Megi (2010). *J. Atmos. Sci.*, **74**, 1169–1200, https://doi.org/10.1175/JAS-D-16-0075.1.

Chen, H., and D.-L. Zhang, 2013: On the rapid intensification of Hurricane Wilma (2005). Part II: Convective bursts and the upper-level warm core. *J. Atmos. Sci.*, **70**, 146–162, https://doi.org/10.1175/JAS-D-12-062.1.

Christophersen, H., A. Aksoy, J. Dunion, and K. Sellwood, 2017: The impact of NASA Global Hawk unmanned aircraft dropwindsonde observations on tropical cyclone track, intensity, and structure: Case studies. *Mon. Wea. Rev.*, **145**, 1817–1830, https://doi.org/10.1175/MWR-D-16-0332.1.

Emanuel, K. A., and F. Zhang, 2017: The role of inner-core moisture in tropical cyclone predictability and practical forecast skill. *J. Atmos. Sci.*, **74**, 2315–2324, https://doi.org/10.1175/JAS-D-17-0008.1.

Fiorino, M., and R. L. Elsberry, 1989: Some aspects of vortex structure related to tropical cyclone motion. *J. Atmos. Sci.*, **46**, 975–990, https://doi.org/10.1175/1520-0469(1989)046<0975:SAOVSR>2.0.CO;2.

Galarneau, T. J., and C. A. Davis, 2013: Diagnosing forecast errors in tropical cyclone motion. *Mon. Wea. Rev.*, **141**, 405–430, https://doi.org/10.1175/MWR-D-12-00071.1.

Gopalakrishnan, S. G., S. Goldenberg, T. Quirino, X. Zhang, F. Marks, K.-S. Yeh, R. Atlas, and V. Tallapragada, 2012: Toward improving high-resolution numerical hurricane forecasting: Influence of model horizontal grid resolution, initialization, and physics. *Wea. Forecasting*, **27**, 647–666, https://doi.org/10.1175/WAF-D-11-00055.1.

——, F. Marks Jr., J. A. Zhang, X. Zhang, J.-W. Bao, and V. Tallapragada, 2013: A study of the impacts of vertical diffusion on the structure and intensity of the tropical cyclones using the high-resolution HWRF system. *J. Atmos. Sci.*, **70**, 524–541, https://doi.org/10.1175/JAS-D-11-0340.1.

Han, J., W. Wang, Y. C. Kwon, S. Hong, V. Tallapragada, and F. Yang, 2017: Updates in the NCEP GFS cumulus convection schemes with scale and aerosol awareness. *Wea. Forecasting*, **32**, 2005–2017, https://doi.org/10.1175/WAF-D-17-0046.1.

Holmlund, K., 1998: The utilization of statistical properties of satellite-derived atmospheric motion vectors to derive quality indicators. *Wea. Forecasting*, **13**, 1093–1104, https://doi.org/10.1175/1520-0434(1998)013<1093:TUOSPO>2.0.CO;2.

Honda, T., S. Kotsuki, G.-Y. Lien, Y. Maejima, K. Okamoto, and T. Miyoshi, 2018: Assimilation of Himawari-8 all-sky radiances every 10 minutes: Impact on precipitation and flood risk prediction. *J. Geophys. Res. Atmos.*, **123**, 965–976, https://doi.org/10.1002/2017JD027096.

Iacono, M. J., J. S. Delamere, E. J. Mlawer, M. W. Shephard, S. A. Clough, and W. D. Collins, 2008: Radiative forcing by long-lived greenhouse gases: Calculations with the AER radiative transfer models. *J. Geophys. Res.*, **113**, D13103, https://doi.org/10.1029/2008JD009944.

Ito, K., 2016: Errors in tropical cyclone intensity forecast by RSMC Tokyo and statistical correction using environmental parameters. *SOLA*, **12**, 247–252, https://doi.org/10.2151/sola.2016-049.

Kanada, S., and A. Wada, 2015: Numerical study on the extremely rapid intensification of an intense tropical cyclone: Typhoon Ida (1958). *J. Atmos. Sci.*, **72**, 4194–4217, https://doi.org/10.1175/JAS-D-14-0247.1.

Kim, H., C. Lozano, V. Tallapragada, D. Iredell, D. Sheinin, H. L. Tolman, V. M. Gerald, and J. Sims, 2014: Performance of ocean simulations in the coupled HWRF–HYCOM Model. *J. Atmos. Oceanic Technol.*, **31**, 545–559, https://doi.org/10.1175/JTECH-D-13-00013.1.

Kim, M., H. M. Kim, J. Kim, S.-M. Kim, C. Velden, and B. Hoover, 2017: Effect of enhanced satellite-derived atmospheric motion vectors on numerical weather prediction in East Asia using an adjoint-based observation impact method. *Wea. Forecasting*, **32**, 579–594, https://doi.org/10.1175/WAF-D-16-0061.1.

Kunii, M., M. Otsuka, K. Shimoji, and H. Seko, 2016: Ensemble data assimilation and forecast experiments for the September 2015 heavy rainfall event in Kanto and Tohoku regions with atmospheric motion vectors from *Himawari-8*. *SOLA*, **12**, 209–214, https://doi.org/10.2151/sola.2016-042.

Kwon, Y. C., S. Lord, B. Lapenta, V. Tallapragada, Q. Liu, and Z. Zhang, 2010: Sensitivity of air-sea exchange coefficients (Cd and Ch) on hurricane intensity. *29th Conf. on Hurricanes and Tropical Meteorology*, Tucson, AZ, Amer. Meteor. Soc., 13C.1, https://ams.confex.com/ams/29Hurricanes/techprogram/paper_167760.htm.

Lim, A. H. N., J. A. Jung, S. E. Nebuda, J. M. Daniels, W. Bresky, M. Tong, and V. Tallapragada, 2019: Tropical cyclone forecasts impact assessment from the assimilation of hourly visible, shortwave, and clear-air water vapor atmospheric motion vectors in HWRF. *Wea. Forecasting*, **34**, 177–198, https://doi.org/10.1175/WAF-D-18-0072.1.

Liu, Q., X. Zhang, S. Trahan, and V. Tallapragada, 2012: Extending operational HWRF initialization to triple-nest HWRF system. *30th Conf. on Hurricanes and Tropical Meteorology,* Ponte Verde, FL, Amer. Meteor. Soc., 14A.6, https://ams.confex.com/ams/30Hurricane/webprogram/Paper204853.html.

Lu, X., X. Wang, Y. Li, M. Tong, and X. Ma, 2017a: GSI-based ensemble-variational hybrid data assimilation for HWRF for hurricane initialization and prediction: Impact of various error covariances for airborne radar observation assimilation. *Quart. J. Roy. Meteor. Soc.*, **143**, 223–239, https://doi.org/10.1002/qj.2914.

——, ——, M. Tong, and V. Tallapragada, 2017b: GSI-based, continuously cycled, dual-resolution hybrid ensemble–variational data assimilation system for HWRF: System description and experiments with Edouard (2014). *Mon. Wea. Rev.*, **145**, 4877–4898, https://doi.org/10.1175/MWR-D-17-0068.1.

Miyamoto, Y., and T. Takemi, 2013: A transition mechanism for the spontaneous axisymmetric intensification of tropical cyclones. *J. Atmos. Sci.*, **70**, 112–129, https://doi.org/10.1175/JAS-D-11-0285.1.

——, and ——, 2015: A triggering mechanism for rapid intensification of tropical cyclones. *J. Atmos. Sci.*, **72**, 2666–2681, https://doi.org/10.1175/JAS-D-14-0193.1.

——, and D. S. Nolan, 2018: Structural changes preceding rapid intensification in tropical cyclones as shown in a large ensemble of idealized simulations. *J. Atmos. Sci.*, **75**, 555–569, https://doi.org/10.1175/JAS-D-17-0177.1.

Neumann, C. J., and J. M. Pelissier, 1981: Models for the prediction of tropical cyclone motion over the North Atlantic: An operational evaluation. *Mon. Wea. Rev.*, **109**, 522–538, https://doi.org/10.1175/1520-0493(1981)109<0522:MFTPOT>2.0.CO;2.

Pan, H. L., and W.-S. Wu, 1995: Implementing a mass flux convective parameterization package for the NMC medium range forecast model. NMC Office Note 409, 40 pp., https://www.emc.ncep.noaa.gov/officenotes/FullTOC.html#1990.

Parrish, D. F., and J. C. Derber, 1992: The National Meteorological Center's Spectral Statistical-Interpolation Analysis System. *Mon. Wea. Rev.*, **120**, 1747–1763, https://doi.org/10.1175/1520-0493(1992)120<1747:TNMCSS>2.0.CO;2.

Pu, Z., S. Zhang, M. Tong, and V. Tallapragada, 2016: Influence of the self-consistent regional ensemble background error covariance on hurricane inner-core data assimilation with the GSI-based hybrid system for HWRF. *J. Atmos. Sci.*, **73**, 4911–4925, https://doi.org/10.1175/JAS-D-16-0017.1.

Rogers, R., P. Reasor, and S. Lorsolo, 2013: Airborne Doppler observations of the inner-core structural differences between intensifying and steady-state tropical cyclones. *Mon. Wea. Rev.*, **141**, 2970–2991, https://doi.org/10.1175/MWR-D-12-00357.1.

RSMC Tokyo-Typhoon Center 2016: Annual report on the activities of the RSMC Tokyo-Typhoon Center 2016. Japan Meteorological Agency, 95 pp., http://www.jma.go.jp/jma/jma-eng/jma-center/rsmc-hp-pub-eg/AnnualReport/2016/Text/Text2016.pdf.

Shimada, U., K. Aonashi, and Y. Miyamoto, 2017: Tropical cyclone intensity change and axisymmetricity deduced from GSMaP. *Mon. Wea. Rev.*, **145**, 1003–1017, https://doi.org/10.1175/MWR-D-16-0244.1.

Shimoji, K., 2014: Motion tracking and cloud height assignment methods for Himawari-8 AMV. *Proc. 12th Int. Winds Workshop*, Copenhagen, Denmark, CIMSS, University of Wisconsin–Madison, 37 pp., http://cimss.ssec.wisc.edu/iwwg/iww12/talks/01_Monday/1710_IWWG_0616_2_algorithm_Shimoji_final.pdf.

Tallapragada, V., C. Kieu, Y. Kwon, S. Trahan, Q. Liu, Z. Zhang, and I. Kwon, 2014: Evaluation of storm structure from the operational HWRF during 2012 implementation. *Mon. Wea. Rev.*, **142**, 4308–4325, https://doi.org/10.1175/MWR-D-13-00010.1.

——, and Coauthors, 2015: Forecasting tropical cyclones in the western North Pacific basin using the NCEP Operational HWRF: Real-time implementation in 2012. *Wea. Forecasting*, **30**, 1355–1373, https://doi.org/10.1175/WAF-D-14-00138.1.

——, and Coauthors, 2016: Forecasting tropical cyclones in the western North Pacific basin using the NCEP Operational HWRF Model: Model upgrades and evaluation of real-time performance in 2013. *Wea. Forecasting*, **31**, 877–894, https://doi.org/10.1175/WAF-D-14-00139.1.

Tong, M., and Coauthors, 2018: Impact of assimilating aircraft reconnaissance observations on tropical cyclone initialization and prediction using operational HWRF and GSI ensemble–variational hybrid data assimilation. *Mon. Wea. Rev.*, **146**, 4155–4177, https://doi.org/10.1175/MWR-D-17-0380.1.

Torn, R. D., 2014: The impact of targeted dropwindsonde observations on tropical cyclone intensity forecasts of four weak systems during PREDICT. *Mon. Wea. Rev.*, **142**, 2860–2878, https://doi.org/10.1175/MWR-D-13-00284.1.

Velden, C., and Coauthors, 2005: Recent innovations in deriving tropospheric winds from meteorological satellites. *Bull. Amer. Meteor. Soc.*, **86**, 205–224, https://doi.org/10.1175/BAMS-86-2-205.

——, W. E. Lewis, W. Bresky, D. Stettner, J. Daniels, and S. Wanzong, 2017: Assimilation of high-resolution satellite-derived atmospheric motion vectors: Impact on HWRF forecasts of tropical cyclone track and intensity. *Mon. Wea. Rev.*, **145**, 1107–1125, https://doi.org/10.1175/MWR-D-16-0229.1.

Wu, T., H. Liu, S. J. Majumdar, C. S. Velden, and J. L. Anderson, 2014: Influence of assimilating satellite-derived atmospheric motion vector observations on numerical analyses and forecasts of tropical cyclone track and intensity. *Mon. Wea. Rev.*, **142**, 49–71, https://doi.org/10.1175/MWR-D-13-00023.1.

——, C. S. Velden, S. J. Majumdar, H. Liu, and J. L. Anderson, 2015: Understanding the influence of assimilating subsets of enhanced atmospheric motion vectors on numerical analyses and forecasts of tropical cyclone track and intensity with an ensemble Kalman filter. *Mon. Wea. Rev.*, **143**, 2506–2531, https://doi.org/10.1175/MWR-D-14-00220.1.

Wu, W., R. J. Purser, and D. F. Parrish, 2002: Three-dimensional variational analysis with spatially inhomogeneous covariances. *Mon. Wea. Rev.*, **130**, 2905–2916, https://doi.org/10.1175/1520-0493(2002)130<2905:TDVAWS>2.0.CO;2.

Yablonsky, R. M., I. Ginis, B. Thomas, V. Tallapragada, D. Sheinin, and L. Bernardet, 2015: Description and analysis of the ocean component of NOAA's Operational Hurricane Weather Research and Forecasting Model (HWRF). *J. Atmos. Oceanic Technol.*, **32**, 144–163, https://doi.org/10.1175/JTECH-D-14-00063.1.

Yamaguchi, M., T. Nakazawa, and K. Aonashi, 2012: Tropical cyclone track forecasts using JMA model with ECMWF and JMA initial conditions. *Geophys. Res. Lett.*, **39**, L09801, https://doi.org/10.1029/2012GL051473.

——, J. Ishida, H. Sato, and M. Nakagawa, 2017: WGNE intercomparison of tropical cyclone forecasts by operational NWP models: A quarter century and beyond. *Bull. Amer. Meteor. Soc.*, **98**, 2337–2349, https://doi.org/10.1175/BAMS-D-16-0133.1.

Yamashita, K., 2016: Assimilation of Himawari-8 atmospheric motion vectors into JMA's operational global, mesoscale and local NWP systems. *CAS/JSC WGNE Res. Activ. Atmos. Oceanic Modell.*, **46**, 01.33–01.34.

Zhang, D.-L., and H. Chen, 2012: Importance of the upper-level warm core in the rapid intensification of a tropical cyclone. *Geophys. Res. Lett.*, **39**, L02806, https://doi.org/10.1029/2011GL050578.

Zhang, J. A., D. S. Nolan, R. F. Rogers, and V. Tallapragada, 2015: Evaluating the impact of improvements in the boundary layer parameterization on hurricane intensity and structure forecasts in HWRF. *Mon. Wea. Rev.*, **143**, 3136–3155, https://doi.org/10.1175/MWR-D-14-00339.1.

Zhang, S., Z. Pu, and C. Velden, 2018: Impact of enhanced atmospheric motion vectors on HWRF hurricane analyses and forecasts with different data assimilation configurations. *Mon. Wea. Rev.*, **146**, 1549–1569, https://doi.org/10.1175/MWR-D-17-0136.1.